

Manifold Model for High-Resolution fMRI Joint Reconstruction and Dynamic Quantification

Shouchang Guo, Jeffrey A. Fessler, *Fellow, IEEE*, and Douglas C. Noll, *Senior Member, IEEE*

Abstract—Oscillating Steady-State Imaging (OSSI) is a recent fMRI acquisition method that exploits a large and oscillating signal, and can provide high SNR fMRI. However, the oscillatory nature of the signal leads to an increased number of acquisitions. To improve temporal resolution and accurately model the nonlinearity of OSSI signals, we build the MR physics for OSSI signal generation as a regularizer for the undersampled reconstruction rather than using subspace models that are not well suited for the data. Our proposed physics-based manifold model turns the disadvantages of OSSI acquisition into advantages and enables joint reconstruction and quantification. OSSI manifold model (OSSIMM) outperforms subspace models and reconstructs high-resolution fMRI images with a factor of 12 acceleration and without spatial or temporal resolution smoothing. Furthermore, OSSIMM can dynamically quantify important physics parameters, including R_2^* maps, with a temporal resolution of 150 ms.

Index Terms—Manifold model, high-resolution fMRI, quantitative MRI, R_2^* , oscillating steady-state imaging (OSSI), joint reconstruction and quantification.

I. INTRODUCTION

Functional magnetic resonance imaging (fMRI) is an important tool for brain research and diagnosis. In its most common form, it detects functional activation by acquiring a time-series of MR images with blood-oxygen-level-dependent (BOLD) contrast [1]. However, the BOLD effect has a relatively low signal-to-noise ratio (SNR) [2], and the SNR further decreases with improved spatial resolution. Because the functional units (cortical columns) of the brain are on the order of 1 mm, high resolution with high SNR is critical for some fMRI experiments. This paper focuses on Oscillating Steady-State Imaging (OSSI), a recent fMRI acquisition approach that provides higher SNR signals than standard gradient-echo (GRE) imaging [3].

The SNR advantage of OSSI comes at a price of spatial and temporal resolutions. OSSI acquisition requires a quadratic RF phase cycling with cycle length n_c (e.g., $n_c = 10$). The corresponding OSSI signal oscillates with a periodicity of $n_c \cdot TR$, and the frequency-dependent oscillations result in oscillatory patterns in OSSI images. Therefore, every image in a regular fMRI time course is acquired n_c times with different phase increments in OSSI, and combining the n_c

images eliminates oscillations for fMRI analysis. Acquiring n_c times more images compromises temporal resolution, and the short TR necessary for OSSI acquisition can limit single-shot spatial resolution.

To improve the spatial-temporal resolution, we previously used a patch-tensor low-rank model for the sparsely undersampled reconstruction [4]. While low-rank regularization fits data to linear subspaces, OSSI images are not very low-rank because of the nonlinear oscillations [5]. Instead of imposing low-rankness and/or sparsity that may or may not suit the data, this paper proposes a nonlinear dimension reduction approach for OSSI reconstruction that uses a MR physics-based manifold as a regularizer, inspired by parameter map reconstruction methods for MR fingerprinting [6], [7].

As outlined in Fig. 1, the manifold model focuses on MR physics for OSSI signal generation. It represents n_c OSSI signal values per voxel by just 3 physical parameters, via Bloch equations. The nonlinear nature of the Bloch equations enables nonlinear representations of the data and nonlinear dimension reduction. We further introduce a near-manifold regularizer that encourages the reconstructed signal values to lie near the manifold. Compared to quantitative imaging works that enforce the reconstructed images to be exactly equal to the physics-based representations [6]–[9], the proposed near-manifold regularizer encourages the images to be near the manifold while also allowing for potential model mismatch.

Standard T_2^* -weighted magnitude images only assess relative signal changes due to BOLD effects and are not quantitative in terms of the blood oxygenation level, T_2^* or T_2' [10]–[12]. Quantifying T_2^* is important because of its sensitivity to iron concentration for disease monitoring [13]. By constructing a T_2' manifold based on BOLD-induced intravoxel dephasing, our work demonstrates the utility of the OSSI manifold model for dynamic quantification of T_2^*/R_2^* .

This paper shows that the proposed T_2' manifold and near-manifold regularizer can jointly optimize OSSI images and quantitative maps. The manifold model enables high-resolution OSSI fMRI with 12-fold acquisition acceleration, outperforms low-rank regularization with more functional activation, and provides quantitative and dynamic assessment of tissue R_2^* maps and off-resonance f_0 , with a temporal resolution of 150 ms.

II. OSSI MANIFOLD MODEL (OSSIMM)

OSSI signal oscillates with a periodicity of $n_c TR$, and the OSSI fMRI time course contains n_c images for every image in a regular fMRI time series. We refer to the fast acquisition

This work was supported by National Institute of Biomedical Imaging and Bioengineering (NIBIB) and National Institute of Neurological Disorders and Stroke (NINDS) through grants R01 EB023618 and U01 EB026977.

S. Guo and J. A. Fessler are with the Department of Electrical Engineering and Computer Science, University of Michigan, Ann Arbor, MI 48109 USA (e-mail: shoucguo@umich.edu, fessler@umich.edu).

D. C. Noll is with the Department of Biomedical Engineering, University of Michigan, Ann Arbor, MI 48109 USA (e-mail: dnoll@umich.edu).

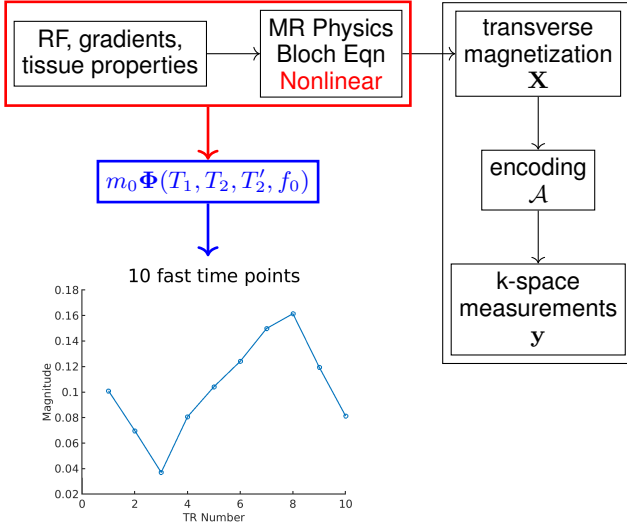


Fig. 1: The proposed manifold model uses the MR physics for signal generation as a regularizer for the undersampled reconstruction.

dimension of size n_c as “fast time” and the regular fMRI time dimension as “slow time” as presented in supplemental Fig. S10. OSSI fast time signals can have different shapes and change nonlinearly with respect to MR physics parameters, as illustrated in Fig. 2. To accurately model the nonlinear oscillations, we propose a MR-physics based manifold model for the undersampled reconstruction.

A. Physics-Based Manifold

In OSSI, the steady-state transverse magnetization of one isocromat at observation time t is

$$m_0 \phi(t; T_1, T_2, f_0),$$

where $m_0 \in \mathbb{C}$ is the equilibrium magnetization, $\phi(\cdot) \in \mathbb{C}^{n_c}$ represents MR physics calculated by Bloch equations, T_1 and T_2 are tissue relaxation times, and f_0 denotes central off-resonance frequency from B_0 field inhomogeneity.

T_2' -weighted OSSI signal in a voxel with an intra-voxel spreading of off-resonance frequencies f can be modeled as:

$$m_0 \Phi(t; T_1, T_2, T_2', f_0) = \int m_0 \phi(t; T_1, T_2, f_0 + f) p(f; T_2') df. \quad (1)$$

The T_2' exponential decay corresponds to a Cauchy distribution for f with a probability density function (PDF) $p(f) = \gamma/\pi(\gamma^2 + f^2)$, and scale parameter $\gamma = 1/(2\pi T_2')$.

The isocromat signal at time $t > 0$ presents increased T_2 decay and increased off-resonance dephasing due to field inhomogeneity and BOLD-related field changes,

$$m_0 \phi(t; T_1, T_2, f_0) = m_0 \phi(t = 0; T_1, T_2, f_0) e^{-t/T_2} e^{-i2\pi f_0 t}, \quad (2)$$

where $t = 0$ denotes the time right after the excitation.

As OSSI TR is relatively short (e.g., TR = 15 ms), we neglect the intravoxel dephasing during the readout and approximate the signal at $0 \leq t \leq \text{TR}$ with the signal at the echo time TE. The T_2' -weighted signal becomes

$$m_0 \Phi(T_1, T_2, T_2', f_0) \approx \int m_0 \phi(\text{TE}; T_1, T_2, f_0 + f) e^{-\text{TE}/T_2} e^{-i2\pi(f_0+f)\text{TE}} p(f; T_2') df. \quad (3)$$

Accordingly, T_2' -weighted OSSI fast time signals lie on the physics-based manifold:

$$\{m_0 \Phi(T_1, T_2, T_2', f_0) \in \mathbb{C}^{n_c} : m_0 \in \mathbb{C}, T_1, T_2, T_2', f_0 \in \mathbb{R}\}, \quad (4)$$

The manifold maps a limited number of physics parameters to the n_c -dimensional oscillating signals via MR physics.

B. Near-Manifold Regularization

The physics-based manifold models the generation of MR signals, enables nonlinear dimension reduction, and can be an accurate prior for the undersampled reconstruction. Because the physics parameters are location dependent, and because OSSI signal values change drastically with varying parameters as shown in Fig. 2, we model the fast time signals in a voxel-by-voxel manner. Furthermore, to account for potential mismatches due to model simplifications and nonidealities in experiments (e.g., flip angle inhomogeneity), we propose a near-manifold regularizer that encourages the signal values in each voxel to be close to the manifold estimates but not necessarily exactly the same.

The proposed T_2' manifold-based image reconstruction problem uses the following optimization formulation:

$$\hat{\mathbf{X}} = \arg \min_{\mathbf{X}} \frac{1}{2} \|\mathcal{A}(\mathbf{X}) - \mathbf{y}\|_2^2 + \beta \sum_{n=1}^N \mathcal{R}(\mathbf{X}[n, :]),$$

$$\mathcal{R}(\mathbf{v}) = \min_{m_0, T_2', f_0} \|\mathbf{v} - m_0 \Phi(T_2', f_0; T_1, T_2)\|_2^2, \quad (5)$$

where $\mathbf{X} \in \mathbb{C}^{N \times n_c}$ denotes n_c fast time images to be reconstructed. The vectorized spatial dimension N is N_{xy} for 2D OSSI fMRI. $\mathcal{A}(\cdot)$ is a linear operator consisting of coil sensitivities and the non-uniform Fourier transform including undersampling, \mathbf{y} represents sparsely sampled k-space measurements. β is the regularization parameter. $\mathbf{v} \in \mathbb{C}^{n_c}$ is a vector of fast time signal values for each voxel in \mathbf{X} , $m_0 \Phi(T_2', f_0; T_1, T_2) \in \mathbb{C}^{n_c}$ denotes the manifold estimates. The regularizer minimizes the Euclidean distance between \mathbf{v} and $m_0 \Phi(T_2', f_0; T_1, T_2)$. T_1 and T_2 are not directly estimated by the model. T_1 has a signal scaling effect that can be absorbed in m_0 , as illustrated in Fig. 2. Section III describes the choices of baseline T_2 values for T_2' estimation.

The voxel-wise parametric regularizer $\mathcal{R}(\mathbf{v})$ not only performs regularization for the ill-posed reconstruction problem, but also involves parameter estimation and can provide quantitative maps for T_2' and f_0 .

C. Optimization Algorithm

To solve (5), we alternate between a regularization update and a data fidelity update for the reconstruction. The

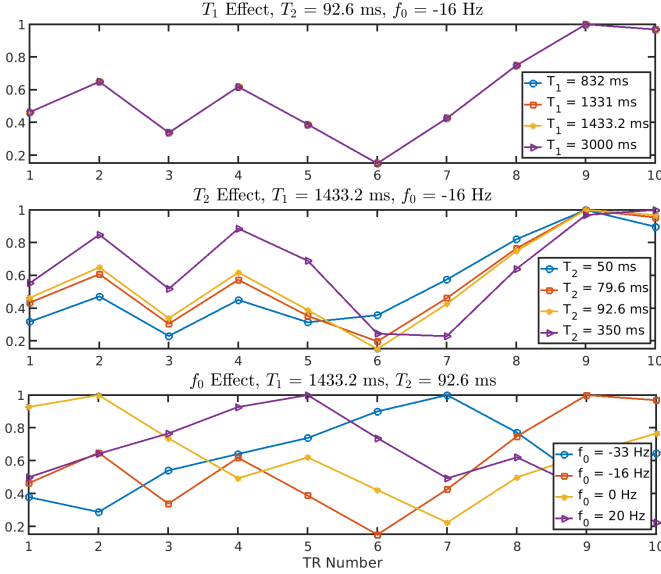


Fig. 2: Normalized OSSI fast time signal magnitude for one isocromat with nonlinear oscillations determined by physics parameters T_2 and f_0 . The change of T_1 only scales OSSI signal values.

minimization of the voxel-wise parametric regularizer is a nonlinear least-square problem that we solve using the variable projection (VARPRO) method [14], [15]. Let $\theta = [T_2', f_0]$ denote the two nonlinear tissue parameters; the calculation of θ using VARPRO simplifies to

$$\hat{\theta} = \arg \max_{\theta} \frac{|\Phi(\theta)'v|^2}{\|\Phi(\theta)\|_2^2}, \quad (6)$$

where $v = X[:, n] \in \mathbb{C}^{n_c}$. Instead of solving (6) for the explicit and sophisticated $\Phi(\theta)$, we construct a dictionary consisting of discrete $\Phi(\theta)$ realizations with varying θ parameters using Bloch simulations, and then perform grid search to find $\hat{\theta}$ for which $\Phi(\hat{\theta})$ best matches v .

Updating m_0 is a least-squares problem with closed-form solution:

$$\hat{m}_0 = \frac{\Phi(\hat{\theta})'v}{\|\Phi(\hat{\theta})\|_2}. \quad (7)$$

We parallelize the regularization update across different voxels.

The update step for X involves a quadratic least-squares problem that we solve using the conjugate gradient method as implemented in the Michigan Image Reconstruction Toolbox [16]. This data fidelity update is easily parallelized over different fast time images or different fast time image sets to speed up the fMRI time series reconstruction.

D. Comparison Method

We compare the manifold approach to a low-rank reconstruction approach that models the fast time signals using linear subspaces. The cost function for this low-rank comparison method is

$$\hat{X} = \arg \min_X \frac{1}{2} \|\mathcal{A}(X) - y\|_2^2 + \alpha \|X\|_* \quad (8)$$

where $X \in \mathbb{C}^{N \times n_c}$ represents every n_c fast time images, and α is the regularization parameter. We solve the optimization problem (8) using the proximal optimized gradient method (POGM) with adaptive restart [17]–[19].

III. SIMULATION INVESTIGATIONS

We generated OSSI signals via Bloch simulation using pulse-sequence parameters that matched the actual data acquisition. We used TR = 15 ms, TE = 2.7 ms (spiral-out trajectory), RF excitation pulse length = 1.6 ms, quadratic RF phase cycling with $\Phi(n) = \pi n^2/n_c$ for n th TR, $n_c = 10$, and flip angle = 10° [3].

A. OSSI Signals

The OSSI signal $\in \mathbb{C}^{n_c}$ for one isocromat is determined by physics parameters T_1 , T_2 , and f_0 . Fig. 2 presents example OSSI isocromat signals (normalized by the maximum magnitude) with varying physics parameters selected based on gray matter relaxation parameters: $T_1 = 1400$ ms, $T_2 = 92.6$ ms [20]. As an approximation of (3), we simulated T_2' -weighted OSSI signal in a voxel with Riemann sum of numerous OSSI isocromat signals at different off-resonance frequencies. Specifically, we calculated a weighted sum of OSSI signals from 4000 isocromats at off-resonance frequency $f_0 + f$, where f uniformly ranged from -200 Hz to 200 Hz, and the weighting function was the PDF of the Cauchy distribution.

We further simulated a fMRI time course for one voxel with time-varying T_2' values. The T_2' waveform is the convolution of the canonical hemodynamic response function (HRF) [21] and the fMRI task waveform. Because fMRI percent signal change $\Delta\% \approx \Delta R_2' \cdot TE_{\text{eff}}$ [22] and OSSI $TE_{\text{eff}} = 17.5$ ms [3], we set $\Delta T_2' = 15.4$ ms to produce a typical percent signal change of 2%. The fMRI time course is also affected by scanner drift and respiration induced f_0 changes. We simulated f_0 with a linearly increasing scanner drift of about 1 Hz per minute and a sinusoidal waveform (magnitude of 0.5 Hz and period of 4.2 s) to model the respiratory changes. We also added complex Gaussian random noise for a typical temporal SNR (tSNR) value of 38 dB.

B. Dictionary Selection

We represented OSSI manifold using a signal dictionary, and each dictionary atom is a point on the manifold. Because T_2 , T_2' , and f_0 affect OSSI signals in different ways while T_1 has a scaling effect, we constructed a 4D dictionary by varying T_2 , T_2' , f_0 , for $T_1 = 1400$ ms. The T_2 grids were in the 40 to 150 ms range with a 1 ms spacing. The T_2' grids were calculated by uniformly changing R_2^* from 12 to 38 Hz [23] with a step size of 0.1 Hz and a fixed T_2 of 92.6 ms. We set central off-resonance frequency f_0 to $[-33.3, 33.3]$ Hz with a 0.22 Hz spacing as OSSI signals are periodic with off-resonance frequency period = $1/\text{TR} = 66.7$ Hz [3].

We reconstructed the functional signal and physics parameters from the simulated noisy fMRI time courses using the near-manifold regularizer in (5) and the 4D dictionary. The reconstructions were performed by (a) simultaneously

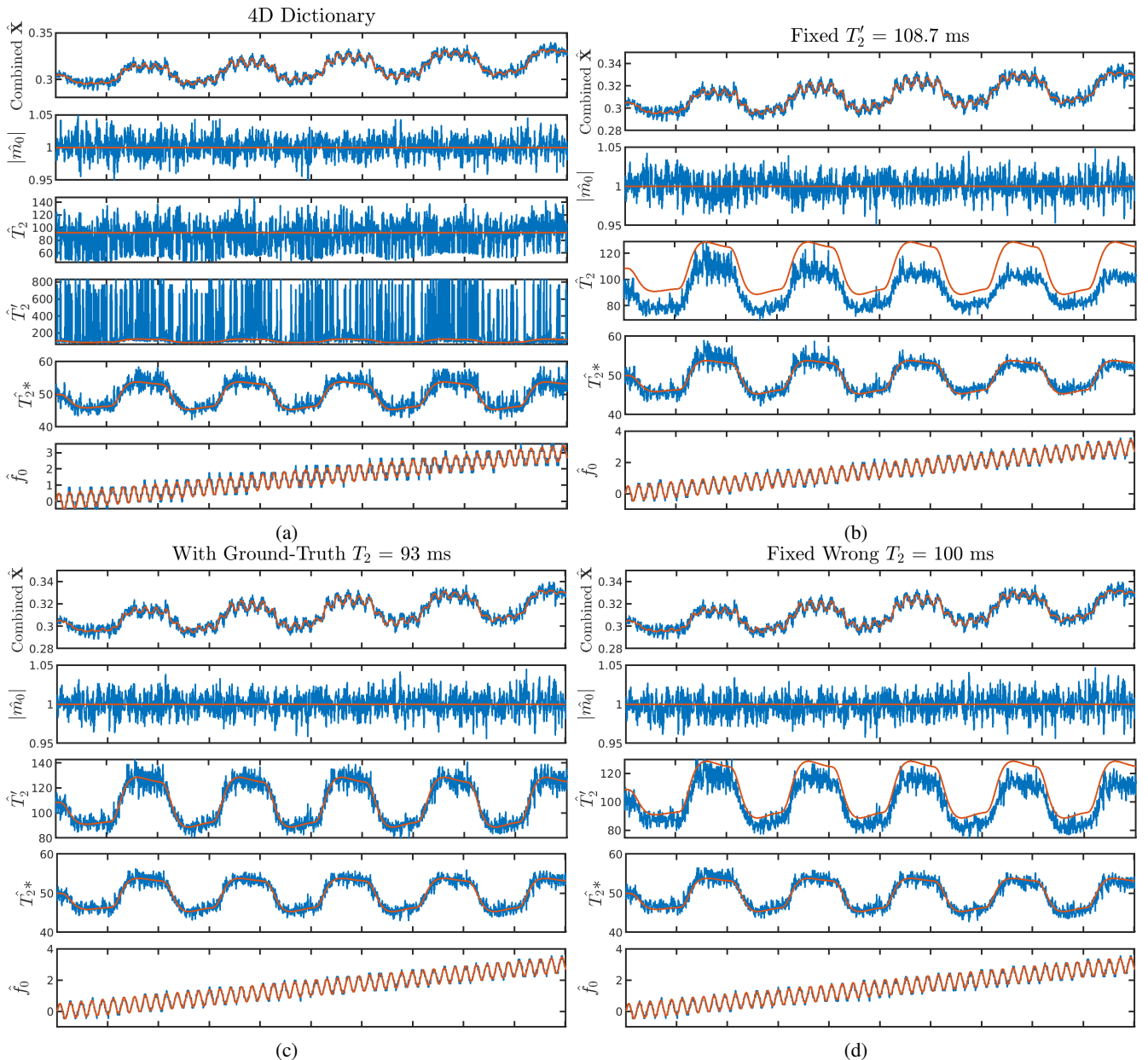


Fig. 3: Quantification results for a simulated OSSI fMRI voxel using the manifold model with 4 different choices of the manifold. Because T_2 and T_2' effects to OSSI signals are correlated (Fig. 3a), and a T_2 manifold is not good enough for capturing BOLD-induced T_2' changes (Fig. 3b), we use a T_2' manifold for quantification. We can estimate T_2^* and T_2' with known T_2 values (Fig. 3c), or use a biased guess of T_2 for quantifying T_2^* (Fig. 3d).

estimating T_2 and T_2' using the 4D dictionary, (b) assuming T_2' is fixed and estimating T_2 using the 3D subset of the 4D dictionary based on the assumed T_2' value, (c) estimating T_2' with the actual T_2 value and the corresponding 3D dictionary, (d) assuming T_2 is fixed and estimating T_2' with a biased T_2 value and the corresponding 3D dictionary.

As shown in Fig. 3, because of the strong coupling between T_2 and T_2' values, it is infeasible to simultaneously estimate T_2 and T_2' (see Fig. 3a). Using a biased T_2' value for T_2 estimation (Fig. 3b) or a biased T_2 value for dynamic T_2' estimation (Fig. 3d) results in noticeable bias, whereas Fig. 3c presents accurate T_2' when the ground truth T_2 is provided. However,

all the different estimation approaches lead to relatively good T_2^* estimates. Because m_0 and T_2^* estimates are more accurate in Figs. 3c and 3d, we propose to use assumed T_2 values or to measure accurate baseline T_2 maps to use for dynamic T_2^* quantification. The latter approach also provides T_2' estimates. Notably, the quality of the combined functional signals is insensitive to the choice of manifold for reconstruction.

IV. EXPERIMENTS

We collected resolution phantom data and human fMRI data to evaluate the potential of the manifold model for joint reconstruction and quantification. All the data were acquired

with a 3T GE MR750 scanner (GE Healthcare, Waukesha, WI) and a 32-channel head coil (Nova Medical, Wilmington, MA).

A. Data Acquisition

OSSI acquisition parameters were the same as in Simulation Investigations with 10 s discarded data points to ensure the steady state. We selected a 2D oblique slice passing through the visual cortex with $\text{FOV} = 220 \times 220 \times 2.5 \text{ mm}^3$, matrix size = $168 \times 168 \times 1$, and spatial resolution = $1.3 \times 1.3 \times 2.5 \text{ mm}^3$. For OSSI, both “mostly sampled” data (for retrospective undersampling) and prospectively undersampled data were acquired. The sampling trajectories were undersampled VD spirals with golden-angle based rotations between time frames as in [4]. The “mostly sampled” data used number of interleaves $n_i = 9$ VD spirals with approximately a 1.5 undersampling factor, and temporal resolution = $1.35 \text{ s} = \text{TR} \cdot n_c \cdot n_i$. The retrospective undersampling used the first interleave out of 9 for each time frame of the “mostly sampled” data. The prospective undersampling used $n_i = 1$ with temporal resolution = $150 \text{ ms} = \text{TR} \cdot n_c$. Both retrospective and prospective undersampling provided $12\times$ acceleration.

For quantification evaluation, we acquired multi-echo GRE images to get standard estimations of f_0 and R_2^* values. GRE images were collected with a spin-warp sequence with $\text{TR} = 100 \text{ ms}$, Ernst flip angle = 16° , and different TEs = 5.9, 13, 26, and 40 ms. R_2^* maps were estimated based on the exponential decay of T_2^* . The field map f_0 was estimated using fully sampled GRE images at TE = 30 and 32 ms [24]. For the phantom data, we additionally acquired spin-echo images with a spin-warp sequence at $\text{TR} = 400 \text{ ms}$ and different TEs = 20, 40, 60, and 80 ms to get \hat{T}_2 maps.

For coil sensitivity map calculation, we collected spin-warp images and generated ESPIRiT sensitivity [25], [26] after compressing the 32-channel coil images to 16 virtual coils using PCA [27]. The coil images were 2-norm combined for brain region extraction using the Brain Extraction Tool [28].

For human data, the functional task was a left vs. right reversing-checkerboard visual stimulus with 10 s rest followed by 5 cycles of left or right stimulus (20 s L/20 s R \times 5 cycles). The 10 s resting-state data ensured the oscillating steady state and were discarded. The number of time frames (both fast time n_c and slow time) was 1490 for “mostly sampled” data and was 13340 for prospectively undersampled data.

B. Performance Evaluation

Every non-overlapping set of $n_c = 10$ fast time images were reconstructed and 2-norm combined for fMRI analysis. To avoid modeling error from the HRF of the initial rest period, the data for the first 40 s task block were discarded. The data were detrended using the first 4 discrete cosine transform basis functions to reduce effects of scanner drift.

We evaluated the functional performance of OSSIMM and comparison approaches using activation maps and tSNR maps. The backgrounds of activation maps were the mean of time-series of images. The activated regions of activation maps were determined by correlation coefficients above a 0.45 threshold. The correlation coefficients were generated by correlating the

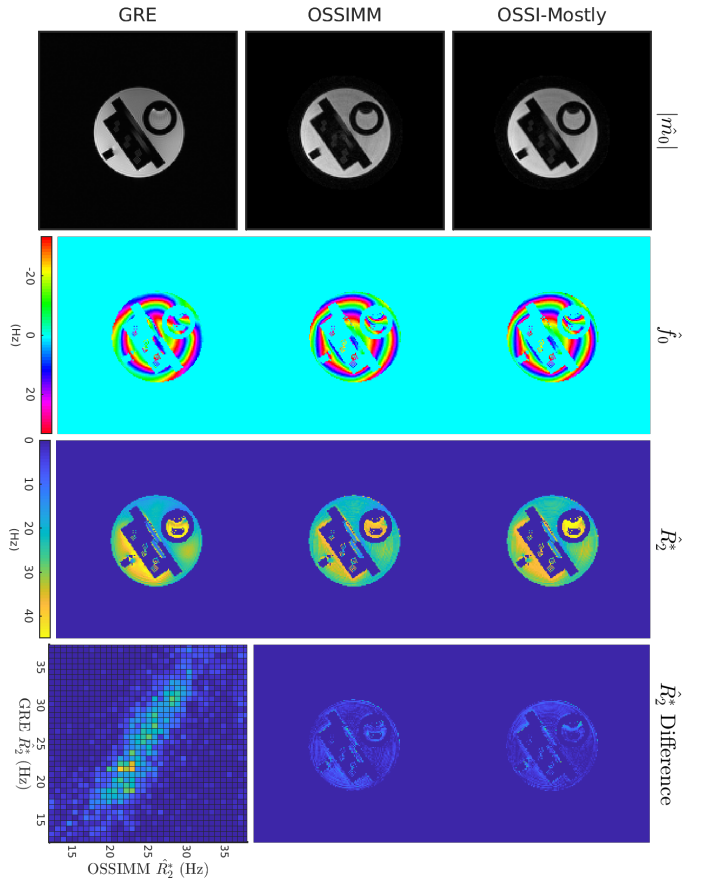


Fig. 4: Phantom quantification of m_0 , f_0 , and R_2^* from mostly sampled OSSI data, retrospectively undersampled OSSI data (reconstructed and quantified using OSSIMM), and multi-echo GRE. The \hat{m}_0 estimates are on arbitrary scales. The GRE \hat{R}_2^* map is used as the standard for difference map calculation. The \hat{R}_2^* maps and \hat{R}_2^* difference maps use the same color scale. The 2D histogram (bottom right) compares OSSIMM and GRE \hat{R}_2^* within the 12-38 Hz range. OSSI \hat{R}_2^* and GRE \hat{R}_2^* demonstrates similar contrasts.

reference waveform (task and HRF related) with the fMRI time course for each voxel. For each voxel, dividing the mean of the time course by the standard deviation of the time course residual (mean and task removed) provided the tSNR map. We further calculated numbers of activated voxels at the bottom third of the brain (where the visual cortex is located) and the average tSNR values within the brain (after skull stripping).

For quantification, parameter estimations at regions with little or no signal are masked out. Specifically, we generated a mask with the first-echo GRE image (TE = 5.9 ms and after skull stripping) for signals larger than 10% of the signal magnitude and GRE $\hat{R}_2^* < 50 \text{ Hz}$. Regions with GRE $\hat{R}_2^* > 50 \text{ Hz}$ are concentrated at the edge of the brain as shown in Fig. S11. The quantitative accuracy of OSSI \hat{R}_2^* was evaluated by RMSE with multi-echo GRE \hat{R}_2^* as the standard. Because OSSI \hat{f}_0 estimates are in the range of $[-33.3, 33.3] \text{ Hz}$, we mapped the GRE \hat{f}_0 to the same range for comparison.

TABLE I: Phantom quantification comparison of OSSI \hat{R}_2^* to GRE with or without a known \hat{T}_2 map

	Fixed $T_2 = 100$ ms		Known \hat{T}_2 map	
	\hat{R}_2^* RMSE (Hz)	Additional Mask	\hat{R}_2^* RMSE (Hz)	Additional Mask
OSSI-Mostly	4.9	4.3	5.0	4.6
OSSIMM	5.5	4.6	5.3	4.5

V. RECONSTRUCTION, QUANTIFICATION, AND RESULTS

The proposed OSSIMM method jointly reconstructed high-resolution images and quantitative maps using the near-manifold regularizer. For both phantom and human experiments, we used the T_2' manifold with a fixed $T_2 = 100$ ms unless otherwise specified. After reconstructing fast time images with mostly sampled data (OSSI-Mostly), or other models such as low-rank (OSSI-LR) and regularized cgSENSE (OSSI-cgSENSE), we further estimated their parameter maps via dictionary fitting using the same manifold as in OSSIMM.

A. Implementation Details

We selected the regularization parameters based on the spectral norm $\sigma(\mathcal{A})$ calculated with power iteration. We set the regularization parameter β in (5) to be a fraction of $\sigma(\mathcal{A})$ such that the condition number of the cost function was about 10 to 20 and the performance of functional maps is maximized. We selected α in (8) to enforce that matrix rank of $\hat{\mathbf{X}}$ was ≈ 4 for most fast-time image sets and to maximize the functional performance.

In OSSIMM, we used 4 iterations of alternating minimization, and 2 iterations of conjugate gradient for the data fidelity update. We used 15 iterations of POGM for the LR reconstruction and 19 iterations of conjugate gradient for cgSENSE reconstruction of undersampled and mostly sampled data. We generated data-shared images as initialization for the undersampled reconstructions by using the sampling incoherence between fast and slow time [4] and combining k-space data of every 10 slow time points.

B. Results

For the phantom study, Fig. 4 and Fig. S12 present OSSI quantification results with a fixed T_2 of 100 ms and a known \hat{T}_2 map, respectively. OSSIMM quantifies parameters from retrospectively undersampled data, and results in similar maps as mostly sampled reconstruction and multi-echo GRE. The 2D histogram demonstrates a close to a linear relationship between OSSI and GRE \hat{R}_2^* values. As summarized in Table I, OSSIMM with a known \hat{T}_2 map produces similar results as OSSIMM with a fixed T_2 value. Demonstrated by RMSE values with additional masking in Table I, OSSI \hat{R}_2^* RMSE improves by 0.5-1 Hz when a GRE $12 < \hat{R}_2^* < 38$ mask (within OSSIMM R_2^* dictionary range) is applied.

Figure 5 compares retrospectively undersampled reconstructions to the mostly sampled reference. OSSIMM reconstruction well preserves high-resolution structures in oscillatory fast

time images and combined images, and leads to less residual in the difference map than LR and cgSENSE approaches.

Figure 6 presents prospectively undersampled reconstructions (temporal resolution = 150 ms) using OSSIMM, LR, and cgSENSE. OSSIMM demonstrates activation map with more activated voxels, time course with higher SNR, and sharper tSNR map than other methods. The functional maps from the mostly sampled reconstruction (temporal resolution = 1.35 s) are included in supplemental Fig. S13 for reference.

Figure 7 gives retrospectively undersampled and mostly sampled OSSI quantification results with comparison to multi-echo GRE. OSSIMM with $12\times$ undersampling leads to \hat{m}_0 , \hat{f}_0 , and \hat{R}_2^* estimates that are almost identical to the mostly sampled case and have finer structures than OSSI-LR. OSSIMM also provides comparable \hat{R}_2^* maps to GRE and demonstrates a similar distribution of \hat{R}_2^* values within the brain as GRE according to the 2D histogram. Because of field drift and respiratory changes between different scans, the OSSI-Mostly and OSSIMM \hat{f}_0 maps are close to GRE \hat{f}_0 but not exactly the same.

Figure 8 compares prospectively undersampled quantification results to multi-echo GRE. OSSIMM enables high-resolution quantification of m_0 , R_2^* and f_0 with a 150 ms acquisition, and yields parameter estimates more similar to GRE than LR and cgSENSE reconstructions.

The parameter maps in Figs. 7 and 8 are from a single set of $n_c = 10$ fast time images, while OSSIMM jointly reconstructs undersampled measurements and quantifies physics parameters for every 10 fast time images of the OSSI fMRI time course. To demonstrate the dynamic quantification capacity of OSSIMM, Fig. 9 shows activation maps for $\hat{m}_0 \exp(-\hat{R}_2^* \text{TE}_{\text{eff}})$ and \hat{R}_2^* , where \hat{m}_0 and \hat{R}_2^* are quantified using OSSIMM and prospectively undersampled data. OSSI $\text{TE}_{\text{eff}} \approx 17.5$ ms with a 2.6 ms actual TE [3].

The activation maps based on $\hat{m}_0 \exp(-\hat{R}_2^* \text{TE}_{\text{eff}})$ images well preserves R_2^* contrast of OSSI and has the same activated regions as the activation map from 2-norm combined OSSI images (in Fig. 6). The activation map from \hat{R}_2^* maps recovers the activation and reduces false positives (negative activation in the positive activation region and vice versa). The colors of the activation are the opposite of activation in Fig. 6 due to the negative correlation between $m_0 \exp(-R_2^* \text{TE}_{\text{eff}})$ and R_2^* . The mean R_2^* map ($\overline{R_2^*}$) of the time series, when compared to GRE, leads to a smaller RMSE value of 4.4 Hz. The RMSE value = 3.7 Hz with a GRE $12 < \hat{R}_2^* < 38$ Hz mask.

Table II summarizes quantitative evaluations of different sampling schemes and reconstruction models. OSSI \hat{R}_2^* RMSE values compared to GRE for retrospectively (Fig. 7) and prospectively (Fig. 8) undersampling are presented. As demonstrated by RMSE values with additional masking, OSSI RMSE decrease by about 0.5 Hz with the GRE $12 < \hat{R}_2^* < 38$ mask. The last two rows of the table correspond to Fig. 6 and are numbers of activated voxels and average tSNR within the brain for prospectively undersampled reconstructions. The proposed OSSIMM jointly reconstructs high-resolution images with more functional activation and parameter maps with smaller \hat{R}_2^* RMSE than other approaches.

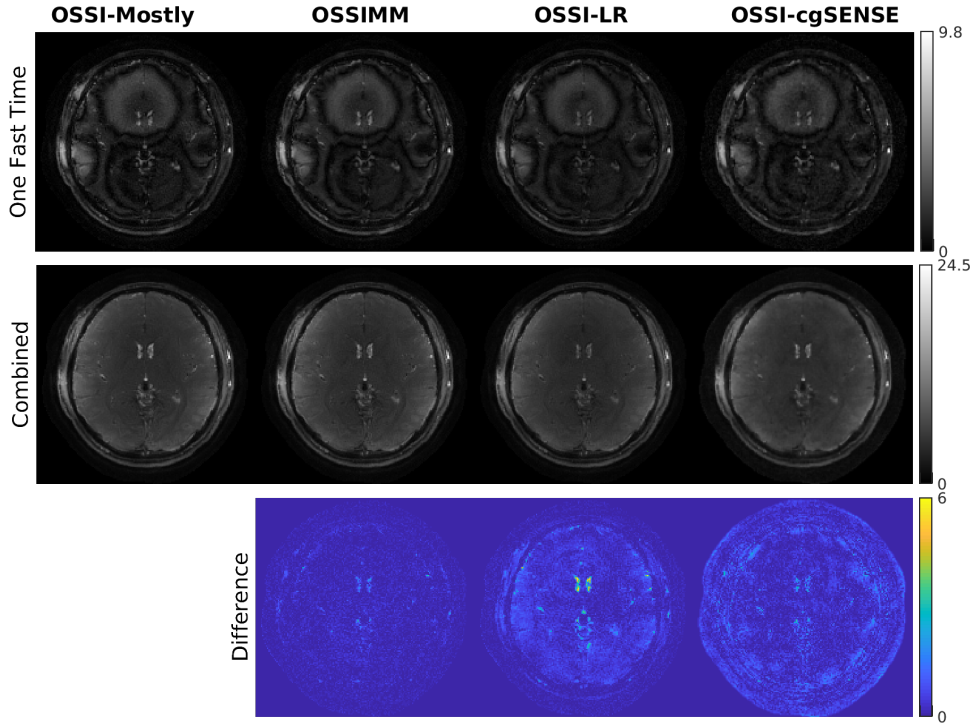


Fig. 5: Manifold, low-rank, and cgSENSE reconstructions for retrospectively undersampled OSSI data are compared to the mostly sampled reconstruction. The example fast time images present spatial variation in OSSI. OSSIMM outperforms other approaches with cleaner high-resolution details and less structure in the difference map.

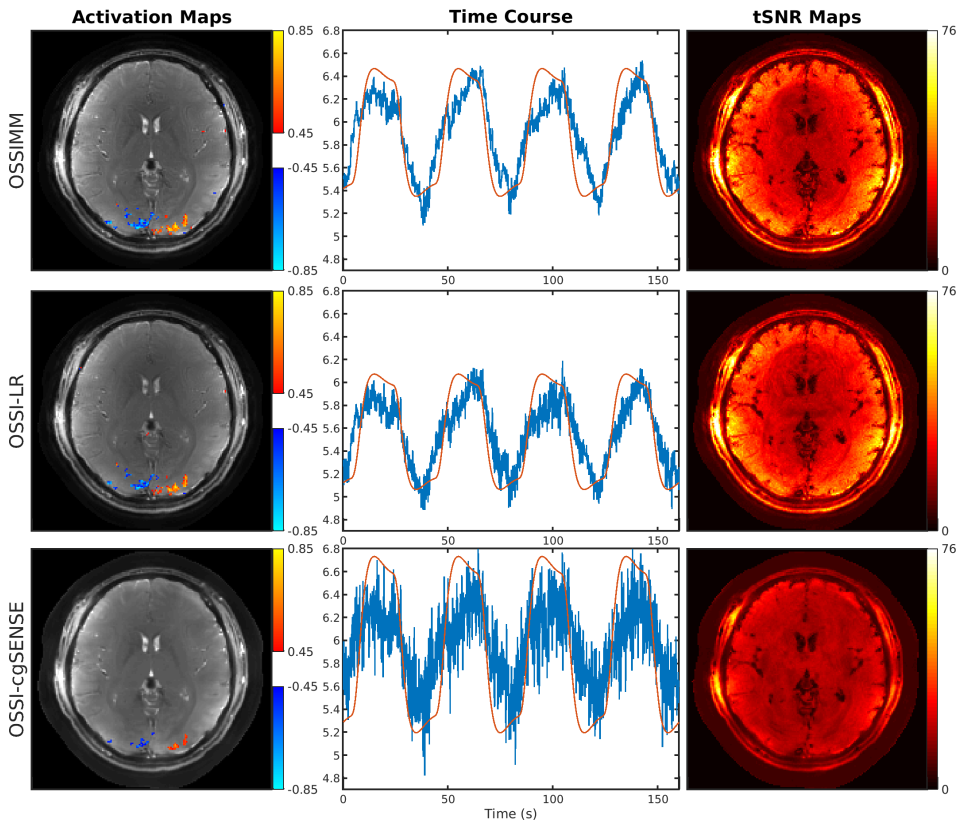


Fig. 6: Functional results for prospectively undersampled data with spatial resolution of 1.3 mm and temporal resolution of 150 ms. The proposed OSSIMM reconstruction provides an activation map with high-resolution background image and larger activated regions, and time course (reference waveform in red) and temporal SNR map with higher SNR than other methods.

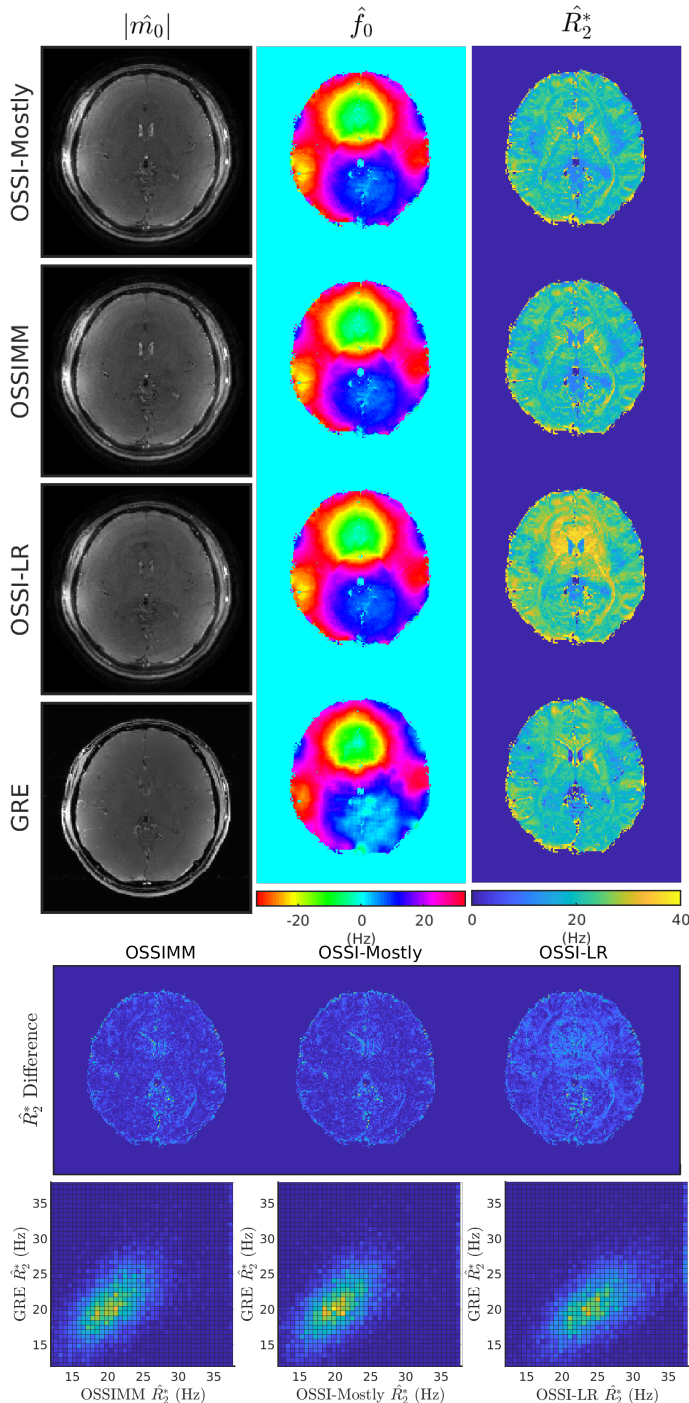


Fig. 7: Retrospectively undersampled quantifications and comparison to multi-echo GRE estimates. OSSIMM presents similar results as the mostly sampled data. \hat{R}_2^* difference maps (using GRE \hat{R}_2^* as standard and of same color scale as \hat{R}_2^* maps) and 2D histogram of \hat{R}_2^* values show that OSSIMM provides comparable quantitative maps to GRE.

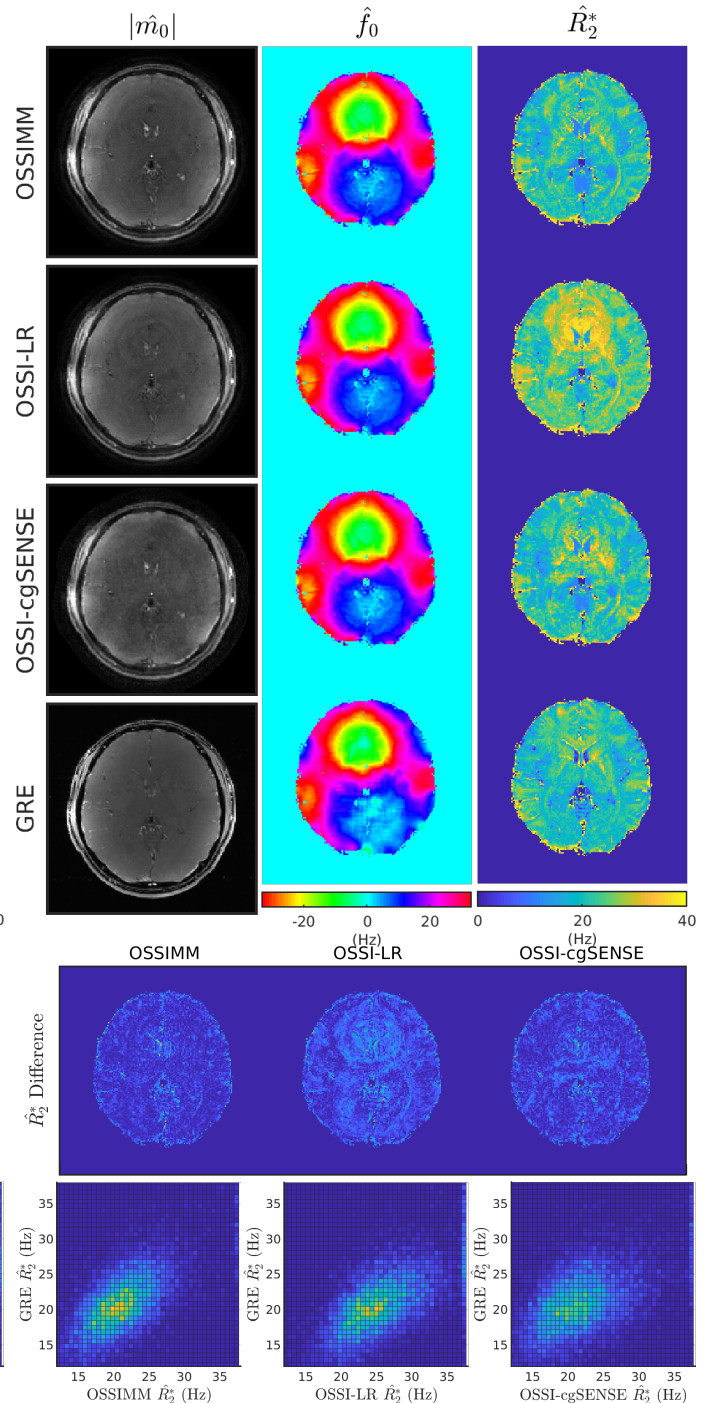


Fig. 8: Prospectively undersampled quantifications compared to multi-echo GRE. OSSIMM results in reasonable parameter maps with 1.3 mm spatial resolution and a 150 ms acquisition time. OSSIMM also outperforms low-rank and cgSENSE reconstructions with less residual in the \hat{R}_2^* difference map (same color scale as \hat{R}_2^* maps).

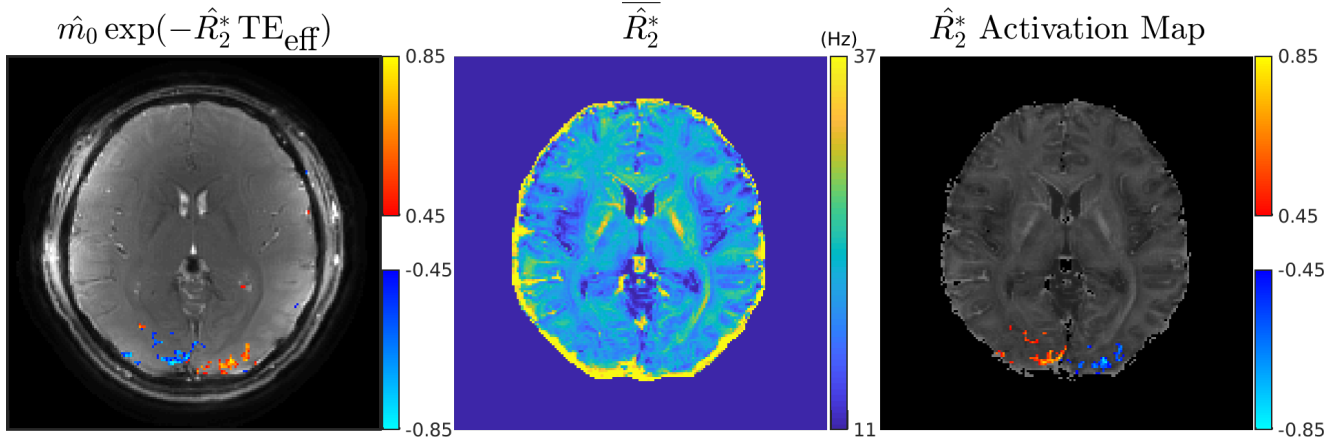


Fig. 9: Activation maps from OSSIMM \hat{m}_0 and \hat{R}_2^* with prospective undersampling demonstrating the dynamic quantification capacity of OSSIMM. Both time series of $\hat{m}_0 \exp(-\hat{R}_2^* TE_{\text{eff}})$ (left) and \hat{R}_2^* (right) almost fully recover the functional activation. The $\overline{\hat{R}_2^*}$ (middle) is the mean of \hat{R}_2^* time series after skull stripping (without any other mask) and well preserves the R_2^* contrast.

TABLE II: Human reconstruction and R_2^* quantification evaluation for different sampling patterns and models

	OSSIMM	OSSI-LR	OSSI-cgSENSE	OSSI-Mostly
Retrospectively Undersampled				
\hat{R}_2^* RMSE (Hz)	5.1	6.6	5.4	5.1
Additional Mask	4.5	6.1	4.9	4.5
Prospectively Undersampled				
\hat{R}_2^* RMSE (Hz)	4.9	6.7	5.5	-
Additional Mask	4.3	6.4	5.0	-
# Activated Voxels	181	159	68	-
Average tSNR	26.4	26.5	18.8	-

VI. DISCUSSION

We propose a novel manifold model OSSIMM that uses MR physics for the signal generation as the regularizer for image reconstruction from undersampled k-space data. The proposed model simultaneously provides high-resolution fMRI images and quantitative maps of important MRI physics parameters.

The proposed near-manifold regularizer has the advantage of allowing for potential imperfections of the manifold model. Instead of requiring the signal values to lie exactly on the manifold, it provides a balance between fitting the fast-time images to the noisy k-space data and to the manifold. For reconstruction, OSSIMM outperforms low-rank and cgSENSE models by providing more functional activation, without spatial or temporal smoothing.

For quantification, OSSIMM dynamically tracks m_0 , R_2^* , and f_0 changes with a temporal resolution of 150 ms in our experiments. The OSSIMM estimates $\hat{m}_0 \exp(-\hat{R}_2^* TE_{\text{eff}})$ or \hat{R}_2^* contain most of the functional information of fMRI time series, and may be well-suited for examining quantitative changes in longitudinal studies. Moreover, OSSIMM quantification is faster than other quantification methods such as [13]. The manifold model and the near-manifold regularization can be

generalized to other sparsely undersampled datasets for joint reconstruction and quantification.

There are multiple factors that contribute to slight mismatches between OSSI \hat{R}_2^* and GRE \hat{R}_2^* . We noticed that OSSI and GRE images were not exactly aligned due to different gradient delays or the movement of the brain between different scans, especially around the edge of the brain. It is also possible that through-plane gradients change signals slightly differently between OSSI and GRE. The OSSIMM implementation could be improved with a larger dictionary with a larger range of R_2^* values and finer spacing of the varying physics parameters. The RF inhomogeneity in the brain may influence the accuracy of the dictionary fitting due to inaccuracy of the flip angle. Alternatively, one might include RF inhomogeneity in the dictionary and fit it as a nuisance parameter.

We have neglected the readout length effect for simplicity and have not performed field map correction for human data. The field map correction improves quantification for resolution phantom, but would increase computation for human fMRI time series. One interesting extension would be to dynamically quantify f_0 and correct for field inhomogeneity using the time-series of OSSI \hat{f}_0 maps. Because OSSI \hat{f}_0 maps are in the range of $[-33.3, 33.3]$ Hz, we could use an initial estimate of \hat{f}_0 from two-echo GRE, and dynamically update the initial \hat{f}_0 based on OSSI \hat{f}_0 changes along time as in [12].

We believe that the reconstruction performance can be further improved with spatial-temporal modeling of OSSI fMRI image series. We will combine OSSIMM with the patch-tensor low-rank model [4] to exploit different aspects of prior information (linear and nonlinear), enlarge the capacity of regularization, and enable more aggressive undersampling. We will also extend the OSSIMM dynamic quantification to 3D fMRI. Because a known \hat{T}_2 map can be helpful for \hat{R}_2^* estimation, one might considering modifying the OSSI sequence as in [13] with slowly varying flip angles and other changes to simultaneously quantify T_2 and T_2' .

VII. CONCLUSION

This paper proposes OSSIMM, a novel reconstruction and quantification model for nonlinear MR signals. With a factor of 12 undersampling and without spatial or temporal smoothing, OSSIMM outperforms other reconstruction models with high-resolution structures and more functional activation. OSSIMM also provides dynamic R_2^* maps that are comparable to GRE \hat{R}_2^* maps with a 150 ms temporal resolution.

ACKNOWLEDGMENT

The authors would like to thank Dr. Amos Cao for important discussions on signal modeling and Dinank Gupta for helping with spin-echo imaging.

REFERENCES

- [1] S. Ogawa, T.-M. Lee, A. S. Nayak, and P. Glynn, "Oxygenation-sensitive contrast in magnetic resonance image of rodent brain at high magnetic fields," *Magnetic resonance in medicine*, vol. 14, no. 1, pp. 68–78, 1990.
- [2] D. C. Noll, "A primer on mri and functional mri," *Technical Report, University of Michigan*, 2001.
- [3] S. Guo and D. C. Noll, "Oscillating steady-state imaging (ossi): A novel method for functional mri," *Magnetic resonance in medicine*, vol. 84, no. 2, pp. 698–712, 2020.
- [4] S. Guo, J. A. Fessler, and D. C. Noll, "High-resolution oscillating steady-state fmri using patch-tensor low-rank reconstruction," *IEEE Transactions on Medical Imaging*, vol. 39, no. 12, pp. 4357–4368, 2020.
- [5] S. Guo, D. C. Noll, and J. A. Fessler, "Dictionary-based oscillating steady state fmri reconstruction," in *Proceedings of the 27th Annual Meeting of ISMRM, Montreal*, 2019, p. 1253.
- [6] B. Zhao, K. Setsompop, H. Ye, S. F. Cauley, and L. L. Wald, "Maximum likelihood reconstruction for magnetic resonance fingerprinting," *IEEE transactions on medical imaging*, vol. 35, no. 8, pp. 1812–1823, 2016.
- [7] J. Assländer, M. A. Cloos, F. Knoll, D. K. Sodickson, J. Hennig, and R. Lattanzi, "Low rank alternating direction method of multipliers reconstruction for mr fingerprinting," *Magnetic resonance in medicine*, vol. 79, no. 1, pp. 83–96, 2018.
- [8] G. Dong, M. Hintermüller, and K. Papafitsoros, "Quantitative magnetic resonance imaging: From fingerprinting to integrated physics-based models," *SIAM Journal on Imaging Sciences*, vol. 12, no. 2, pp. 927–971, 2019.
- [9] J. I. Tamir, F. Ong, S. Anand, E. Karasan, K. Wang, and M. Lustig, "Computational mri with physics-based constraints: Application to multicontrast and quantitative imaging," *IEEE Signal Processing Magazine*, vol. 37, no. 1, pp. 94–104, 2020.
- [10] O. Speck and J. Hennig, "Functional imaging by i0-and t2*-parameter mapping using multi-image epi," *Magnetic resonance in medicine*, vol. 40, no. 2, pp. 243–248, 1998.
- [11] A. B. Wennerberg, T. Jonsson, H. Forsberg, and T.-Q. Li, "A comparative fmri study: T2*-weighted imaging versus r2* mapping," *NMR in Biomedicine: An International Journal Devoted to the Development and Application of Magnetic Resonance In Vivo*, vol. 14, no. 1, pp. 41–47, 2001.
- [12] V. T. Olafsson, D. C. Noll, and J. A. Fessler, "Fast joint reconstruction of dynamic r2* and field maps in functional mri," *IEEE transactions on medical imaging*, vol. 27, no. 9, pp. 1177–1188, 2008.
- [13] C. Y. Wang, S. Coppo, B. B. Mehta, N. Seiberlich, X. Yu, and M. A. Griswold, "Magnetic resonance fingerprinting with quadratic rf phase for measurement of t2* simultaneously with δf , t1, and t2," *Magnetic resonance in medicine*, vol. 81, no. 3, pp. 1849–1862, 2019.
- [14] G. H. Golub and V. Pereyra, "The differentiation of pseudo-inverses and nonlinear least squares problems whose variables separate," *SIAM Journal on numerical analysis*, vol. 10, no. 2, pp. 413–432, 1973.
- [15] G. Golub and V. Pereyra, "Separable nonlinear least squares: the variable projection method and its applications," *Inverse problems*, vol. 19, no. 2, p. R1, 2003.
- [16] J. Fessler, "Michigan image reconstruction toolbox," <https://web.eecs.umich.edu/~fessler/code/index.html>, accessed Jan. 16, 2020.
- [17] D. Kim and J. A. Fessler, "Adaptive restart of the optimized gradient method for convex optimization," *Journal of Optimization Theory and Applications*, vol. 178, no. 1, pp. 240–263, 2018.
- [18] A. B. Taylor, J. M. Hendrickx, and F. Glineur, "Exact worst-case performance of first-order methods for composite convex optimization," *SIAM Journal on Optimization*, vol. 27, no. 3, pp. 1283–1313, 2017.
- [19] C. Y. Lin and J. A. Fessler, "Efficient dynamic parallel MRI reconstruction for the low-rank plus sparse model," *IEEE Trans. Computational Imaging*, vol. 5, no. 1, pp. 17–26, Mar. 2019.
- [20] "Relaxation times," <https://itis.swiss/virtual-population/tissue-properties/database/relaxation-times/>, accessed Jan. 16, 2020.
- [21] "Statistical parametric mapping," <https://www.fil.ion.ucl.ac.uk/spm/>, accessed Jan. 16, 2020.
- [22] T. Jin, P. Wang, M. Tasker, F. Zhao, and S.-G. Kim, "Source of nonlinearity in echo-time-dependent bold fmri," *Magnetic Resonance in Medicine: An Official Journal of the International Society for Magnetic Resonance in Medicine*, vol. 55, no. 6, pp. 1281–1290, 2006.
- [23] P. Péran, G. Hagberg, G. Luccichenti, A. Cherubini, V. Brainovich, P. Celsis, C. Caltagirone, and U. Sabatini, "Voxel-based analysis of r2* maps in the healthy human brain," *Journal of Magnetic Resonance Imaging: An Official Journal of the International Society for Magnetic Resonance in Medicine*, vol. 26, no. 6, pp. 1413–1420, 2007.
- [24] D. C. Noll, J. D. Cohen, C. H. Meyer, and W. Schneider, "Spiral k-space mr imaging of cortical activation," *Journal of Magnetic Resonance Imaging*, vol. 5, no. 1, pp. 49–56, 1995.
- [25] M. Uecker, P. Lai, M. J. Murphy, P. Virtue, M. Elad, J. M. Pauly, S. S. Vasanawala, and M. Lustig, "Espirit—an eigenvalue approach to autocalibrating parallel mri: where sense meets grappa," *Magnetic resonance in medicine*, vol. 71, no. 3, pp. 990–1001, 2014.
- [26] M. Uecker, F. Ong, J. I. Tamir, D. Bahri, P. Virtue, J. Y. Cheng, T. Zhang, and M. Lustig, "Berkeley advanced reconstruction toolbox," in *Proceedings of the 23th Annual Meeting of ISMRM, Montreal*, 2015, p. 2486.
- [27] F. Huang, S. Vijayakumar, Y. Li, S. Hertel, and G. R. Duensing, "A software channel compression technique for faster reconstruction with many channels," *Magnetic resonance imaging*, vol. 26, no. 1, pp. 133–141, 2008.
- [28] S. M. Smith, "Fast robust automated brain extraction," *Human brain mapping*, vol. 17, no. 3, pp. 143–155, 2002.

SUPPLEMENTAL

Figure S10 illustrates OSSI “fast time” and “slow time”. Figure S11 demonstrates voxel locations with GRE $\hat{R}_2^* > 50$ Hz. Figure S12 presents phantom quantification results, and OSSI quantitative maps that were calculated with a known \hat{T}_2 map. Figure S13 presents fMRI results for mostly sampled human data.

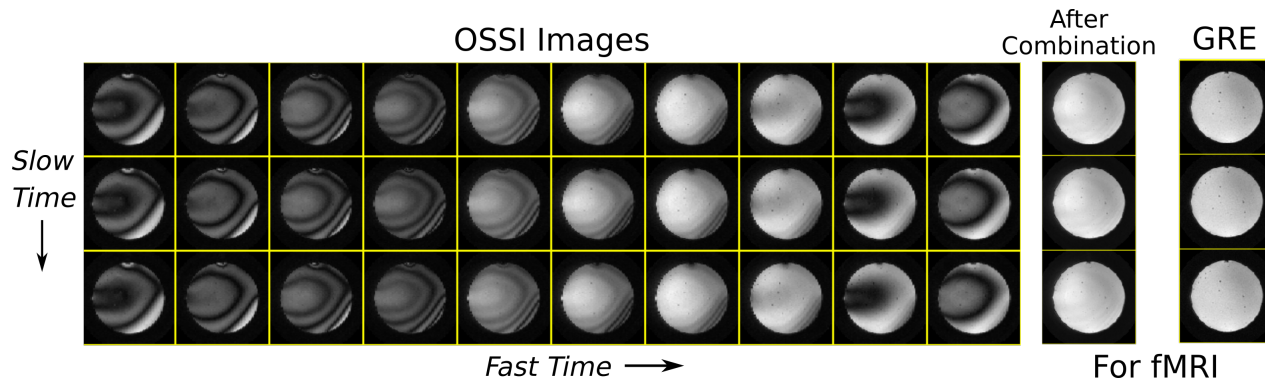


Fig. S10: OSSI images with periodic and nonlinear oscillation patterns are structured along “fast time” and “slow time”. Every n_c fast time images can be 2-norm combined to generate fMRI images that have comparable T_2^* -sensitivity as standard GRE fMRI.

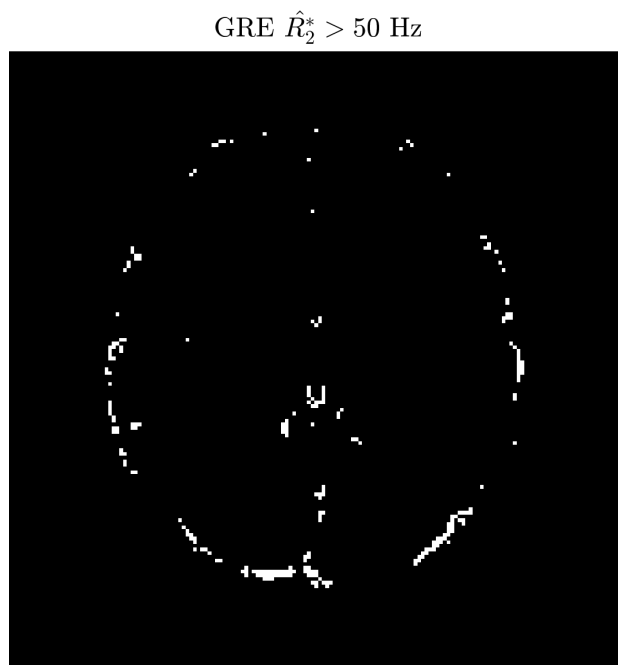


Fig. S11: Most voxel locations with GRE $\hat{R}_2^* > 50$ Hz are around the edges of the brain.

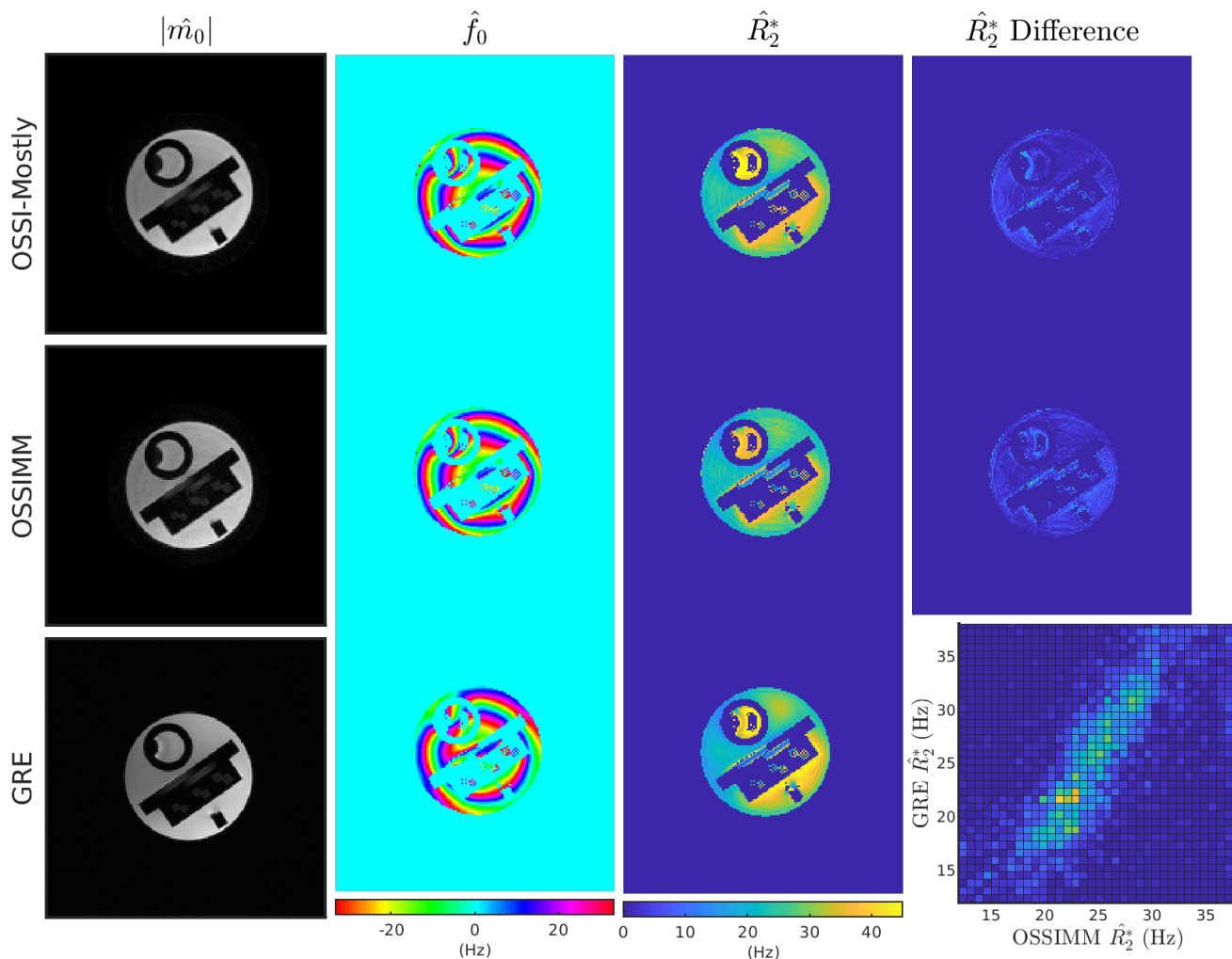


Fig. S12: Phantom quantification of m_0 , f_0 , and R_2^* from mostly sampled OSSI data, retrospectively undersampled OSSI data (reconstructed and quantified using OSSIMM with a known \hat{T}_2 map), and multi-echo GRE. The \hat{m}_0 estimates are on arbitrary scales. The GRE \hat{R}_2^* map is used as the standard for difference map calculation. The \hat{R}_2^* maps and \hat{R}_2^* difference maps use the same color scale. The 2D histogram (bottom right) compares OSSIMM and GRE \hat{R}_2^* within the 12-38 Hz range. OSSIMM \hat{R}_2^* and GRE \hat{R}_2^* have similar contrasts.

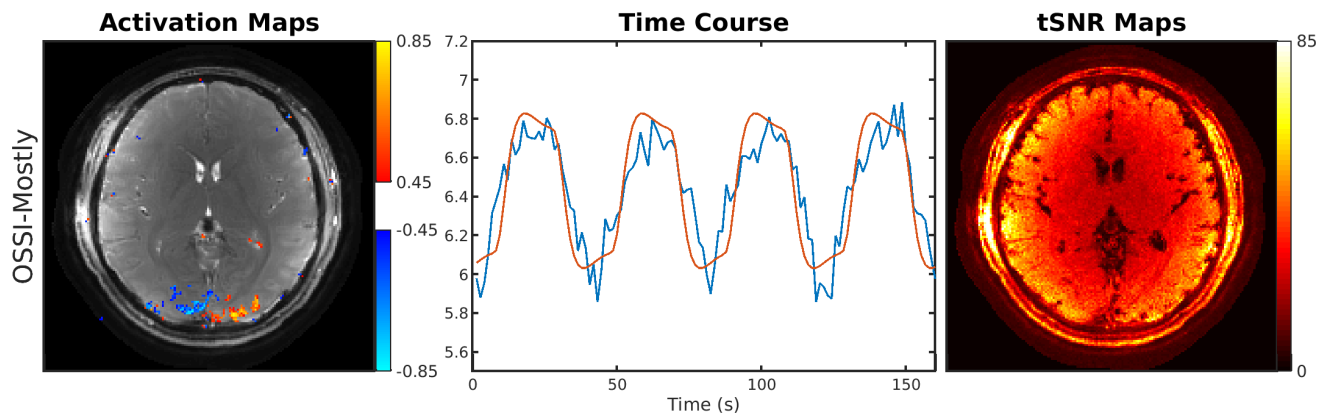


Fig. S13: Functional results for mostly sampled data with spatial resolution of 1.3 mm and temporal resolution of 1.35 s. The number of activated voxels is 236, and the average temporal SNR within the brain is 31.3.